JOURNAL OF GEOPHYSICAL RESEARCH, VOL. 104, NO. D5, PAGES 5697–5716, MARCH 20, 1999

Horizontal wavenumber spectra of winds, temperature, and trace gases during the Pacific Exploratory Missions: 1. Climatology

John Y. N. Cho, Yong Zhu, and Reginald E. Newell

Department of Earth, Atmospheric, and Planetary Sciences, Massachusetts Institute of Technology, Cambridge

Bruce E. Anderson, John D. Barrick, Gerald L. Gregory, and Glen W. Sachse

NASA Langley Research Center, Hampton, Virginia

Mary Anne Carroll[1] and George M. Albercook

Department of Atmospheric, Oceanic, and Space Sciences, University of Michigan, Ann Arbor

Abstract. Aircraft-based meteorological and chemical measurements from NASA's Pacific Exploratory Missions provide a suitable database for studying the climatology of horizontal wavenumber spectra in the troposphere overlying an ocean. The wavenumber spectra of trace gas and meteorological quantities aid in identifying the physical processes producing atmospheric structures as well as provide diagnostics for general circulation models. Flight segments were distributed over altitudes ranging from about $\sim$ 50 m to 13 km and 70°S to 60°N in latitude. The spectra were averaged according to altitude and latitude regions. The wavelength range covered was typically $\sim$ 0.5–100 km. Quantities processed in this way were horizontal velocity, potential temperature, specific humidity, and the mixing ratios of ozone, methane, carbon monoxide, and carbon dioxide. Spectral power and slope (in log-log coordinates) corresponding to the wavelength regime of 6–60 km were tabulated for those measured quantities. The spectral slopes of horizontal velocity and potential temperature were generally close to $-5/3$ with no transition to a steeper slope at short wavelengths as seen in some other studies. Spectral slopes of the tracer species also ranged around $-5/3$. This agreement in form of the dynamical and tracer spectra is consistent with both the gravity-wave advection and quasi two-dimensional turbulence models. In the upper troposphere the spectral power for all quantities except specific humidity tended to be greater at latitudes higher than 30° compared to latitudes lower than 30°. This latitudinal trend confirms the earlier results of the Global Atmospheric Sampling Program.

1. Introduction

The atmosphere is full of structure at all length and timescales. The study of the coupling across different scales is one of the ever-present challenges of atmospheric research; it is a key issue both on a fundamental level and also for applied problems. However, because of the simultaneous existence of multiscaled structure, it is difficult to unravel the interactions between them.

One useful approach is to transform space and time data into wavenumber and frequency domains, effectively decomposing the observation into the parts of its sum, so to speak. One can then compare the distribution of variance density across the wavenumber and frequency spectra to theoretical predictions that are based on different physical models. Perhaps the most famous example of a successful match between such a spectral model and observation is the $k^{-5/3}$ wavenumber power law predicted by *Kolmogorov* [1941] for homogeneous isotropic turbulence. In this case, the prediction of a $-5/3$ power law results simply from dimensional analysis, and the proposition that within a certain length-scale regime (called the inertial subrange) kinetic energy cascades down from large to small eddies without any loss/gain to/from potential energy. The ideas of

[1]Also at the Department of Chemistry, University of Michigan, Ann Arbor.

Paper number 98JD01825.
0148-0227/99/98JD-01825$09.00

universal similarity popularized by Kolmogorov in deriving this spectral form have been applied to describe the characteristics of not only atmospheric turbulence but also of oceanic structures and even of fluctuations in the galactic interstellar medium that span over 12 decades in spatial scale [*Gibson*, 1991].

But however ubiquitously the $-5/3$ power law might appear in wavenumber spectra, three-dimensional turbulence is not necessarily the underlying mechanism producing it. For example, the horizontal wavenumber spectra of kinetic energy in the Earth's atmosphere exhibit a $k^{-5/3}$ behavior at scales of tens and hundreds of kilometers [e.g., *Lilly and Petersen*, 1983] where stratification prevents the vertical development of turbulent eddies anywhere close to those scales. To explain these observations, *Dewan* [1979] proposed a gravity-wave cascade, while *Gage* [1979] and *Lilly* [1983] invoked quasi two-dimensional (stratified) turbulence. Other observations have yielded steeper log-log spectral slopes [e.g., *Myrup*, 1968], which have provoked explanations using buoyancy-modified turbulence [*Bolgiano*, 1962; *Shur*, 1962; *Lumley*, 1964; *Weinstock*, 1978]. More recently gravity-wave theories have been developed for horizontal wavenumber spectra via a similitude approach and a wave cascade [*Dewan*, 1991], a saturated cascade [*Dewan*, 1994, 1997], linear-instability saturation with separable vertical wavenumber and frequency spectra [*Gardner et al.*, 1993] and diffusive filtering [*Gardner*, 1994]. The quasi two-dimensional turbulence ideas have also been further developed for wavenumber spectral predictions [e.g., *Mahalov et al.*, 1998].

For chemical modelers, spatial variability studies such as this one provide a real measure of the fluctuation power at different length scales. At this point in time, even the state-of-the-art atmospheric chemical models work on spatially averaged quantities inside a box with fairly large dimensions. For example, a three-dimensional chemical transport model by *Müller and Brasseur* [1995] uses a $5°\times5°$ latitude-longitude grid with a vertical resolution of 1–2 km in the upper troposphere. Given the high degree of spatial variability in the meteorological and trace gas quantities inside such a box, modelers need to begin taking into account these inhomogeneities. Chemical reaction rates can be highly nonlinear, so the output of an averaged input quantity is not necessarily equal to the averaged output of multiple inputs at finer resolution. Such resolution dependency has shown up quite strongly in model calculations of chemical ozone loss [*Edouard et al.*, 1996]. Recently, *Sparling et al.* [1998] used measured subgrid-scale variance in ClO concentration to estimate the error caused by model calculations that are too coarse to explicitly include such effects. Another good example of this kind of nonlinearity is the dependence of ozone production rate on NO_x, where the rate is positive for an intermediate range of NO_x mixing ratios but negative for values outside of that range [*Brasseur et al.*, 1996]. Using an average value of NO_x abundance within the model box would not produce the correct ozone production rate if there is variability of NO_x within the box. Statistically formed spatial variability spectra of trace gas and meteorological variables could then be used to parameterize the length-scale problem, much like gravity-wave spectra are used as inputs to general circulation models. Measured tracer spectra are also being used as a diagnostic for high-resolution general circulation models [*Strahan and Mahlman*, 1994].

In this paper we present horizontal wavenumber spectra of zonal and meridional velocities (u and v), potential temperature (θ), specific humidity (q), ozone, methane, carbon monoxide, and carbon dioxide mixing ratios calculated from in situ aircraft measurements taken during the NASA Pacific Exploratory Mission (PEM). While the primary purpose of PEM was to provide an assessment of the atmospheric chemistry over the Pacific ocean and to study the effects of emissions from its rim population centers, the large database of high-resolution dynamical and chemical observations it produced is amenable to spectral analysis. Since most of the flights were over the ocean, variability of spectral form due to topographic effects is kept to a minimum. However, the wide range in altitudes at which the aircrafts were flown provides additional information to previous climatological studies.

Here we will focus on the overall statistical averages of each spectral quantity and their variation with respect to altitude and latitude. We will comment on their implications for physical mechanisms in section 5. In subsequent papers we will explore the relationships between the various measured quantities and conduct specific case studies to delve more deeply into the physical mechanisms that generate the observed spectra.

2. Experiment Description

PEM is part of the NASA global tropospheric experiment (GTE) [*McNeal et al.*, 1983] sponsored by the Tropospheric Chemistry Program. There have been three PEMs so far: PEM-West Phase A [*Hoell et al.*, 1996], PEM-West Phase B [*Hoell et al.*, 1997], and PEM-Tropics Phase A [*Hoell et al.*, this issue]. (We will hereafter refer to these three campaigns as PWA, PWB, and PT, respectively.) PWA and PWB were mainly conducted over the northwestern Pacific to study the advection of anthropogenic pollutants from the Asian continent and rim islands and their impact on atmospheric chemistry especially on ozone and the sulfur cycle. PWA was conducted in the fall (1991) when the lower tropospheric flow tended to be ocean-to-continent, while PWB was held in the spring (1994) when the outflow from the Asian continent was maximized. PT was conducted in the late summer/fall (1996) and concentrated on the central and southern Pacific, which are far away from continental sources of chemicals and aerosols. All three missions used a DC-8 as their airborne platform; an additional aircraft (P-3B)

was flown during PT. Figure 1 shows the flight routes during PEM. Note that the DC-8 and P-3B flew mostly different tracks during PT; hereafter, we will refer to the data from the PT DC-8 flights as PTD, and the data from the PT P-3B flights as PTP.

Typically each flight was composed of several straight-and-level tracks at different altitudes connected by steep climbs and descents that were either straight or spiraling. As the marine boundary layer (MBL) was a region of interest, each flight usually contained at least one segment at an altitude $\sim$ 300 m or less. We decided on an arbitrary segment length of $\sim$ 100 km for the spectral transform as a good compromise between getting information on longer-scale ($\sim$ 1000-km) structures and obtaining a sufficient number (i.e., more than several) of spectra for statistical purposes. This places our study more in the length regime covered by *Bacmeister et al.* [1996] than in the length scales of the Global Atmospheric Sampling Program (GASP) [*Nastrom and Gage*, 1985]. Table 1 gives the distribution of the number of straight-and-level flight segments with respect to altitude and latitude. We defined straight-and-level as a flight segment that remained within $\pm$15 m in height and $\pm$7.5° in azimuthal heading. The aircraft navigation system provided the height (pressure altitude) and heading data at a 1-Hz data rate. The DC-8 had a flight ceiling of 12.5 km, while the P-3B had a ceiling of 8.4 km. Because of this difference in performance, the altitude distribution of the flight routes also differed for the two aircraft. For the DC-8, the mode was at 9 km, whereas it was at 5 km for the P-3B. Figure 2 and Figure 3 show this comparison for PT. The cruising air speeds increased with height. The DC-8 had air speeds that varied from $\sim$ 125 m s^{-1} in the MBL to $\sim$ 250 m s^{-1} at the highest altitudes, while the turboprop P-3B air speed ranged from $\sim$ 110 m s^{-1} in the MBL to $\sim$ 160 m s^{-1} at its highest heights.

Of the atmospheric parameters measured during PEM, we chose for this study dynamical and thermal observations as well as trace gas measurements with resolution and continuity suitable for spectral analysis. Hence we have calculated wavenumber spectra of horizontal velocity, potential temperature, specific humidity, and the mixing ratios of ozone, methane, carbon monoxide, and carbon dioxide.

The times and locations of individual flights as well as the complete instrumentation lists including technique used, accuracy, and precision can be found in the ref-

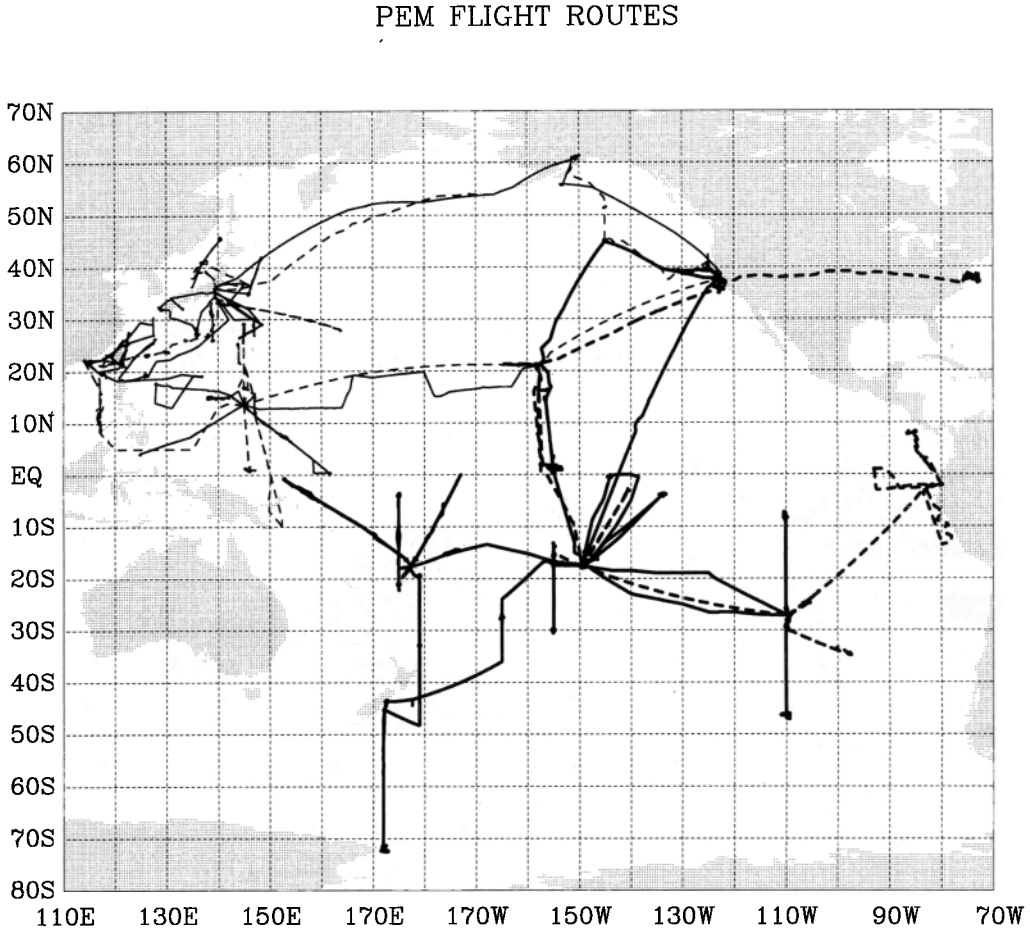

Figure 1. Map of flight tracks flown during the Pacific Exploratory Missions: PEM-West A (thin solid line), PEM-West B (thin dashed line), PEM-Tropics A DC-8 (heavy solid line), and PEM-Tropics A P-3B (heavy dashed line).

Table 1. Number of Straight-and-Level 100-km Flight Segments Versus Altitude and Latitude

Latitude	Mission	$z < 1$ km	1–5 km	5–11 km	> 11 km	Total
> 50°N	PWA	2	3	27	0	32
	PWB	0	5	25	0	30
	Total	2	8	52	0	62
30°–50°N	PWA	8	28	63	53	152
	PWB	30	52	132	17	231
	PTD	2	3	32	0	37
	PTP	5	21	30	0	56
	Total	45	104	257	70	476
10°–30°N	PWA	24	38	144	22	228
	PWB	24	73	205	0	302
	PTD	1	4	24	0	29
	PTP	7	12	37	0	56
	Total	56	127	410	22	615
10°S–10°N	PWA	6	7	34	3	50
	PWB	10	3	63	12	88
	PTD	7	15	86	10	118
	PTP	21	23	29	0	73
	Total	44	48	212	25	329
30°–10°S	PTD	12	35	174	20	241
	PTP	8	37	48	0	93
	Total	20	72	222	20	334
< 30°S	PTD	9	20	64	1	94
	PTP	0	3	9	0	12
	Total	9	23	73	1	106

Grand total = 1922.

erences given in this section for PWA, PWB, and PT. In Table 2 we give the sampling periods and the estimated instrument response times for the data used in this study. The larger values would then be the effective time resolution of the data. Here we give a brief description of each measurement type.

Horizontal velocity was calculated from the heading, ground track, and ground speed data given by the inertial navigation system (Delco Carousel IVA-3 for the DC-8 and Honeywell YG1854 Laseref for the P-3B) and the true air speed derived from the total temperature, static pressure, and differential pressure. Total air tem-

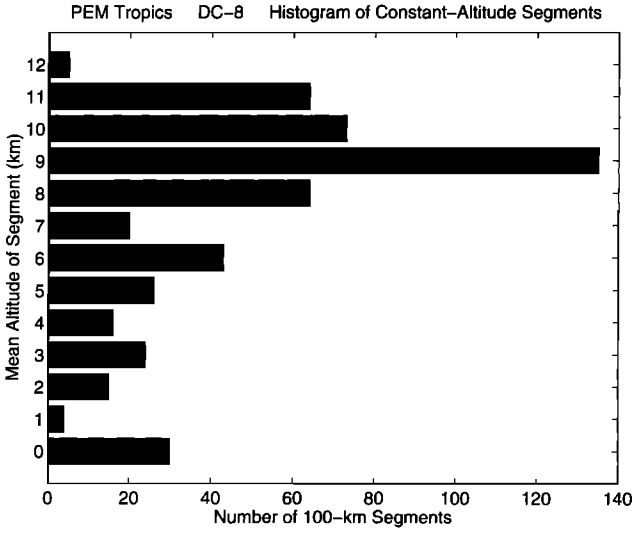

Figure 2. Distribution of straight-and-level 100-km flight segments versus altitude for the DC-8 during PEM Tropics A. The altitudes are rounded off to the nearest kilometer. Thus 0 km includes heights up to 500 m.

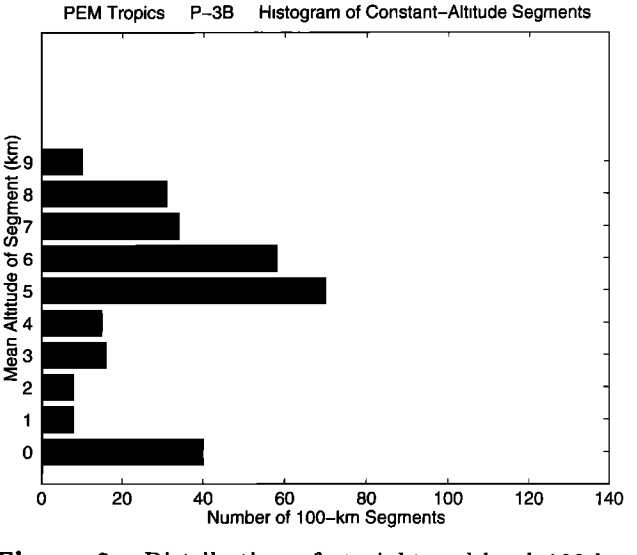

Figure 3. Distribution of straight-and-level 100-km flight segments versus altitude for the P-3B during PEM Tropics A. The altitudes are rounded off to the nearest kilometer. Thus 0 km includes heights up to 500 m.

Table 2. Data Time Resolution

Parameter	PWA	PWB	PTD	PTP
u, v	1 s/1 s [B]	1 s/1 s [B]	1 s/1 s [B]	...
θ	1 s/1 s [B]	1 s/1 s [B]	1 s/1 s [B]	1 s/1 s [B]
q	1 s/2–20 s [B]	1 s/2–20 s [B]	1 s/2–20 s [B]	1 s/2–20 s [B]
O_3	2 s/0.5–1 s [G]	1 s/0.5–1 s [G]	0.5 s/0.5–1 s [G]	1 s/1 s [C]
CH_4	5 s/1 s [S]	1 s/1 s [S]	5 s/1 s [S]	5 s/1 s [S]
CO	5 s/1 s [S]	1 s/1 s [S]	5 s/1 s [S]	5 s/1 s [S]
CO_2	5 s/1 s [G]	1 s/1 s [G]	5 s/1 s [A]	5 s/1 s [A]

For this and all subsequent tables PWA is PEM-West A, PWB is PEM-West B, PTD is PEM-Tropics A DC-8, and PTP is PEM-Tropics A P-3B. The number on the left side of the backslash is the data sampling period, while the number on the right is the estimated instrument response time. Thus the effective data time resolution is the greater of the two numbers. See section 2 for further information. Letters in square brackets denote the principal investigator for the measurement: A is Anderson, B is Barrick, C is Carroll, G is Gregory, and S is Sachse.

perature was measured with a Rosemount 102 AH2Ag system, the static pressure with a Rosemount 1201F2 capacitive sensor, and the differential pressure with a Rosemount 1221F2 capacitive sensor. We estimate the wind speed error to be about ± 1 m s^{-1}, most of it coming from the true air speed instruments. Systematic errors with periods much longer than $\sim$ 15 min were not a problem in this study, since the data segments spectrally analyzed were never longer than 15 min.

Potential temperature was calculated from the static air temperature and the static pressure (0.3% accuracy). The static temperature was calculated from the equation, $T = T_t/(1 + 0.2Ma^2)$, where T_t was the total air temperature (± 1 K accuracy), and $Ma = \{5[(p_d/p + 1)^{5/7} - 1]\}^{1/2}$ was the Mach number calculated from the differential pressure, p_d (0.3% accuracy), and the static pressure; the effects of dynamic heating were thus removed [*Stickney et al.*, 1990]. We chose to use potential temperature instead of temperature to minimize the influence of aircraft bobbing. However, in fact, comparisons of temperature and potential temperature spectra showed only slight differences.

Specific humidity was calculated from the static pressure and the dew/frost point temperature. On the P-3B the dew/frost point was measured by a thermoelectric chilled mirror two-stage hygrometer (GE 1011B: 223–323 K range and 0.5–1 K accuracy). During PWA a three-stage hygrometer (EG&G 300: 198–348 K range and ± 1 K accuracy) was used. For PWB and PTD a composite specific humidity was calculated from the measurements made by the two-stage, three-stage, and a cryogenic chilled mirror system (Buck Research CR-1: 183–303 K range and 0.5–1 K accuracy), which extended the limit of measurement to the highest levels of the DC-8 flights. The composite parameter was dominated by the cryogenic data. The response time varied for each instrument and with dew/frost point. For high dew points the response time was as fast as 2 s, but for low dew/frost points it was as slow as 20 s.

Ozone was measured in situ on the DC-8 employing the $NO + O_3$ chemiluminescence principle [*Clough and Thrush*, 1967]. On the basis of the sample exchange rate at sea level, the response time of the probe was estimated to be $\sim$ 1 s with faster response at higher altitudes. Samples were taken at 5 Hz then averaged to the data resolutions given in Table 2. The same detection principle, although with different hardware [*Ridley et al.*, 1992], was used in the P-3B ozone instrument. Although the inlet line lengths used on some of the flights were quite long ($\sim$ 7 m), which could have degraded the effective time resolution via the differential cross-sectional flow speed within the tube, comparison of spectra for different line lengths showed no appreciable difference in high-wavenumber cutoff behavior. Thus the response time for this instrument also appeared to be $\sim$ 1 s. Ozone data from both instruments were corrected for water-vapor quenching using the humidity measurements.

Methane and carbon monoxide were measured with a diode laser in situ [*Collins et al.*, 1996], using a differential absorption technique. Again, the response time was estimated to be $\sim$ 1 s based on the sample exchange rate. There were quasi-periodic gaps in the data of order 30 s every $\sim$ 10 min due to the real-time calibration procedure.

Carbon dioxide was measured with a nondispersive infrared spectrometer [*Anderson et al.*, 1996]. It shared the gas sampling system with the diode laser. Thus its response time was also $\sim$ 1 s. Except for PWB, however, the archived datasets for CO, CH_4, and CO_2 were 5-s averages.

3. Spectral Analysis Procedure

Each data segment was windowed in the time domain with the Hann (sometimes called "hanning") taper, spectrally transformed using the fast Fourier transform (FFT), then the square of the magnitude taken to

form the frequency spectrum. The mean was subtracted from the data prior to windowing to remove any gross DC bias, but note that the windowing operation generally reintroduces a slight DC component. The Hann window was chosen in order to minimize sidelobe levels in the Fourier domain at the expense of degraded resolution. Since our main interest was in the spectral form rather than in isolated narrow peaks, this choice seemed to be the optimal compromise. The sidelobe suppression was especially critical since we expected "red-noise" power law spectra that rapidly decayed with increasing frequency. A rectangular window, for example, produces spectral sidelobes that fall off only as the square of frequency, so a spectrum steeper than an inverse-square law would be obscured by the windowing artifact. We tested our analysis program with inputs that consisted of Gaussian white noise convolved with finite impulse response filters with power law outputs and found that it worked well in reproducing the expected spectral form for power laws as steep as -4.

The number of FFT points taken varied with the data sampling period, from 1024 for 0.5-s sampling to 128 for 5-s sampling. The idea was to have the time segments span the space-domain equivalent of $\sim$ 100 km. If there were any missing data points within the segment, then it was not used. To provide improved statistical certainty the frequency spectra were smoothed by averaging over different altitude and latitude ranges. They were then transformed to horizontal wavenumber space via Taylor's hypothesis using the mean air speed of the averaging period. Taylor's hypothesis is valid for turbulence, and it should also work well for gravity-wave spectra provided that the aircraft speed was greater than $\sim$ 100 m s^{-1} [*Gardner and Gardner*, 1993], which was true for all our flight segments. However, because the air speed was never perfectly constant, one must expect some "smearing" across the wavenumber bins. Note that this complication also existed for all past aircraft wavenumber spectral analyses of which we are aware.

4. Data Presentation

We begin by showing example spectra from each of the measured quantities. The implications of these observations will be discussed in the section 5. Spectral averages were taken with respect to four altitude regions ($<$ 1 km, 1–5 km, 5–11 km, and $>$ 11 km) and six latitude zones ($<$ 30°S, 30°–10°S, 10°S–10°N, 10°–30°N, 30°–50°N, and $>$ 50°N). Data from all latitudes were used in the height-dependent results, but only data from the 5–11 km altitude bin were used in the latitude-dependent results. We applied this procedure to minimize the injection of height dependency (especially of the MBL region, which was sometimes quite different from the free-tropospheric results) into the latitudinal results. We chose the 5–11 km region because it had the most number of flight segments (Table 1).

For horizontal velocity we were limited to data from the PEM West missions and PTD, because the wind direction data were not of good quality in PTP. Figure 4 displays the horizontal velocity spectra from PWA in the MBL. The solid line is zonal and the dashed line is meridional. Two sample variability bars are included for the zonal spectrum. They are plus/minus twice the standard deviation divided by the square root of the number of spectral averages, i.e., the 95% confidence limit for a normal distribution. Every spectral figure hereafter will include these sample variability bars for the solid line plot. Also, every spectral plot will include a $k^{-5/3}$ line as a guide to the eye.

Horizontal velocity spectra from PTD in the lower troposphere are shown in Figure 5. The spectral slope is steeper than in Figure 4. This was true for all three campaigns for which velocity data are available: The horizontal velocity spectra were steeper in the free atmosphere than in the MBL within each campaign. We shall summarize these kinds of findings in tables later in the paper. Note that the spectra in Figure 4 extend to higher wavenumbers than the spectra in Figure 5 even though the sampling rates were the same for both figures. This was due to the aircraft flying more slowly in the MBL and thus effectively reducing the minimum sampling distance.

In Figure 6 we compare MBL potential temperature spectra from PTD (solid line) and PTP (dashed line). The measurements and parameter calculations were done in the same way, but the platforms were different and the routes flown were not always the same. Note also that because of the difference in aircraft performance, the height distribution of flight segments within the 5–11-km range differed markedly between PTD and PTP (Figure 2 and Figure 3). There is some difference in the spectral powers at higher wavenumbers, but otherwise they are quite consistent. There is a bigger difference in power at higher altitudes, also at higher wavenumbers (Figure 7). In general, the potential temperature spectra had slopes that encompassed $-5/3$ within the bounds of statistical uncertainty regardless of aircraft, altitude, or latitude.

Specific humidity is not a good passive tracer because water vapor can change phase to water and ice. Nevertheless, spatial variability of humidity is of interest in itself. Although the PTD (solid line) and PTP (dashed line) spectra in Figure 8 show good agreement, the PWA and PWB results in the MBL (not shown) were quite different in power. We believe the peak in the PTD curve at the high wavenumber end can be attributed to the heating/cooling time constant for the hygrometers' chilled mirrors, especially for the cryogenic system. Similar peaks showed up at higher altitudes (Figure 9) in the PTD data. However, in any case, the high-wavenumber region (beyond $\sim$ 0.3 km^{-1}) should not be taken at face value because of the slow and variable response times of the dew/frost point instruments, especially at low dew/frost points (generally

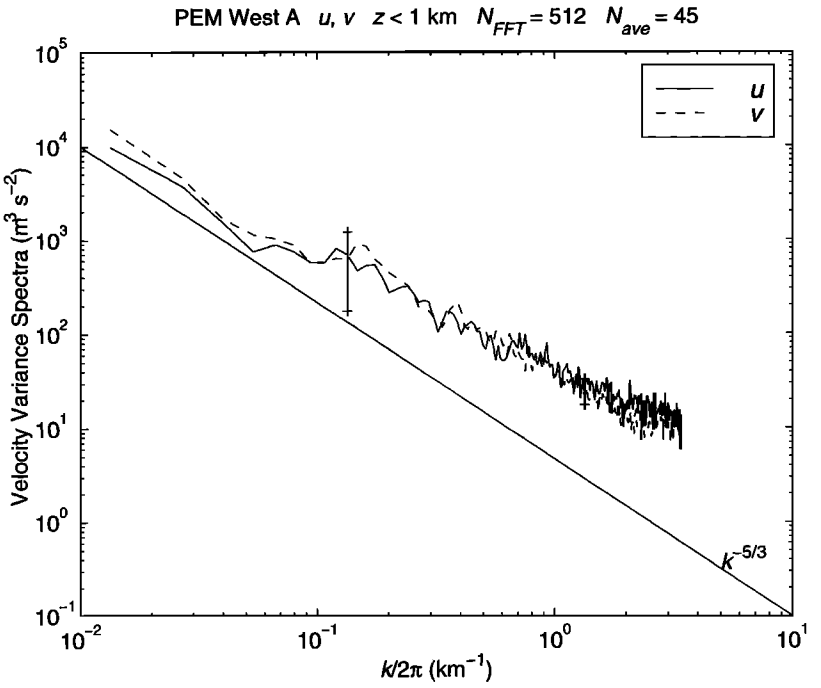

Figure 4. Horizontal wavenumber variance spectra for zonal (solid line) and meridional (dashed line) wind fluctuations. The title above the plot gives the campaign name, data type, altitude range, FFT length, and the number of spectral averages, respectively. Two sample variability bars are shown for the zonal spectrum. They are plus/minus twice the standard deviation divided by the square root of the number of spectral averages.

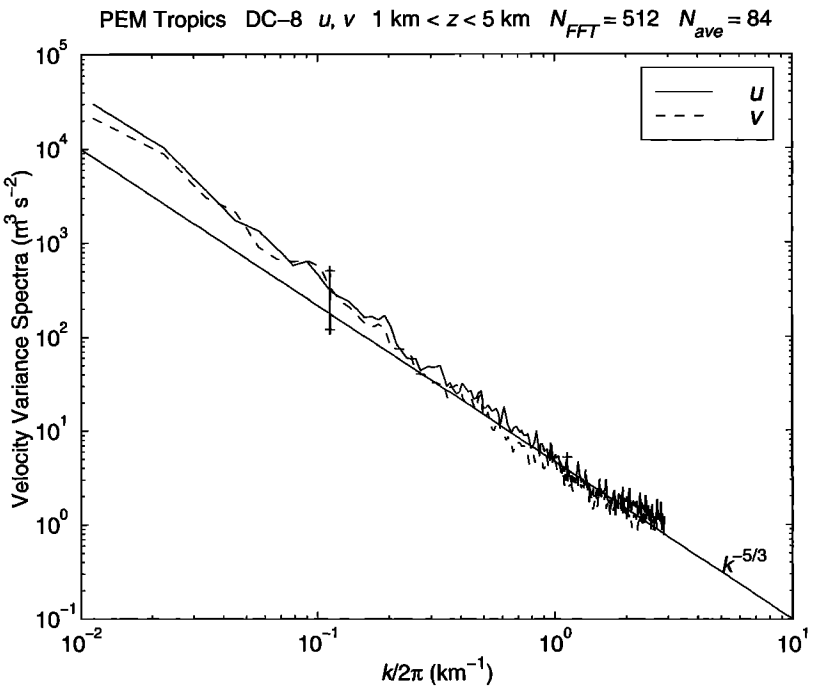

Figure 5. Horizontal wavenumber variance spectra for zonal (solid line) and meridional (dashed line) wind fluctuations. The title above the plot gives the campaign name and aircraft type, data type, altitude range, FFT length, and the number of spectral averages, respectively. See Figure 4 caption for further explanations.

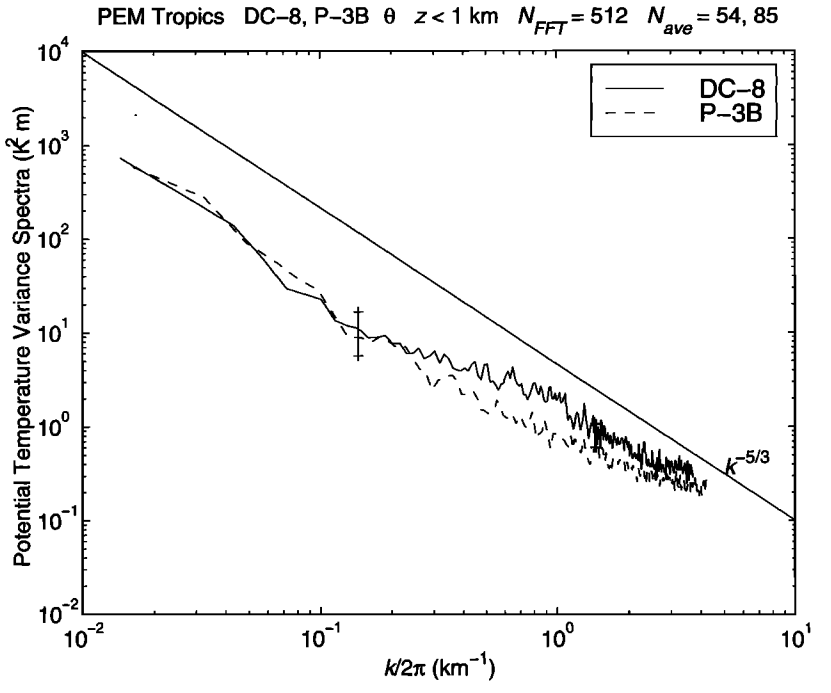

Figure 6. Horizontal wavenumber variance spectra of potential temperature for PTD (solid line) and PTP (dashed line) data. The title above the plot gives the campaign name and aircraft types, data type, altitude range, FFT length, and the number of spectral averages for the PTD and PTP data, respectively. See Figure 4 caption for further explanations.

high altitudes). The steepening of the spectral slopes at high wavenumbers in Figure 9 was most likely the result of the slowness of the chilled mirror response.

The mixing ratio variance spectra of ozone, which should be a better passive tracer than water vapor, were still generally more variable than the velocity and potential temperature spectra but more consistent across platforms and campaigns than the water vapor spectra. Figure 10 displays spectra from PWA (solid line) and PWB (dashed line) in the MBL. They have significantly

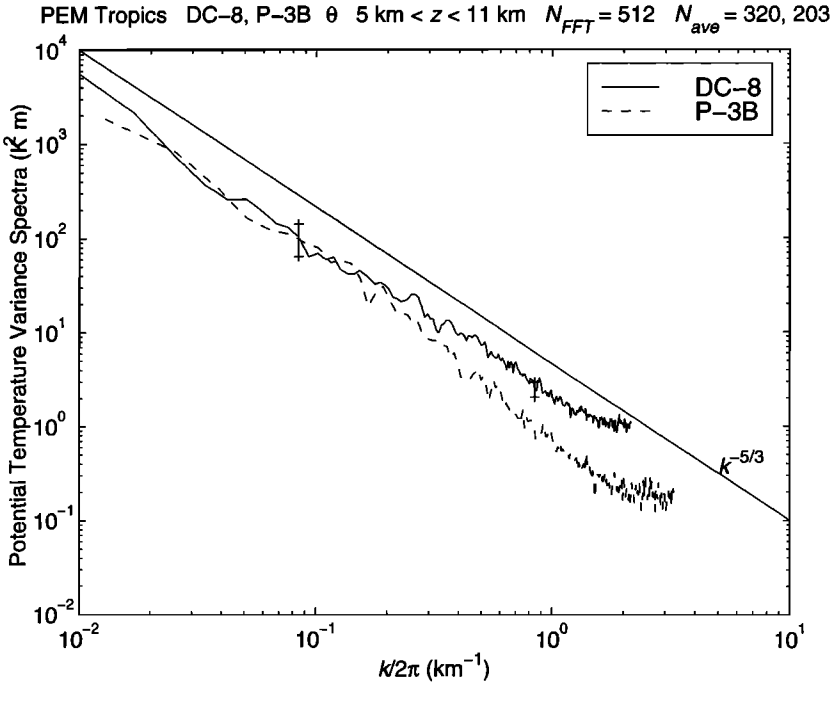

Figure 7. Same as Figure 6, except for an altitude range of 5–11 km.

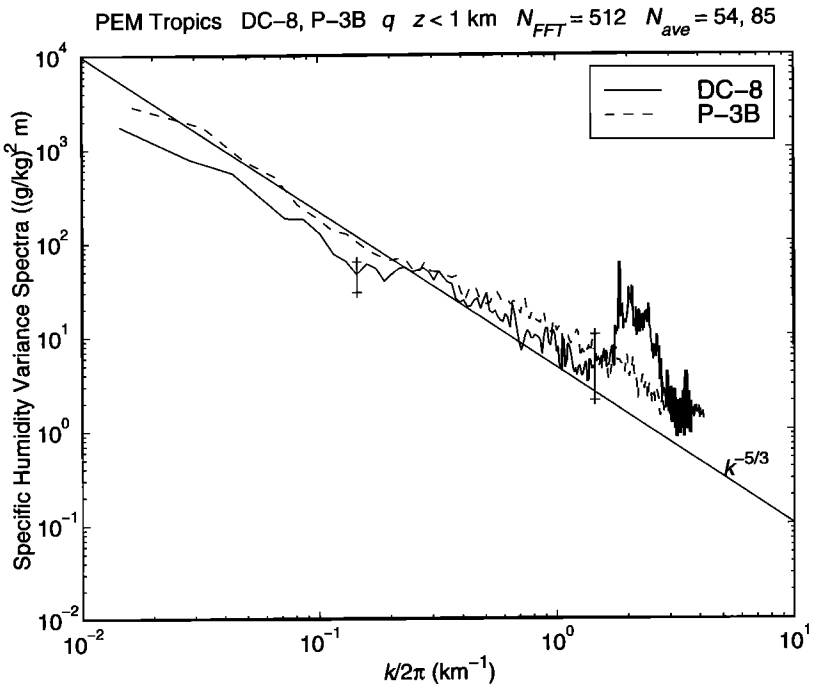

Figure 8. Same as Figure 6, except that the data type is specific humidity.

different forms. Note the extension of the PWB curve to higher wavenumbers because the finer sampling time of the data allowed a higher Nyquist limit. In the 1–5-km range the ozone spectra were more consistent across platforms and campaigns (e.g., Figure 11). Again, the difference in the wavenumber range was due to the different data sampling rate. Note, however, the large spectral peak in the PTD curve at ~ 3 km^{-1}. Because this spectral feature was only present in the PTD data (but consistently so), we believe it was an instrumental or data processing artifact. We are currently investigating this matter.

For the remaining chemical species under analysis here, the data sampling period was 5 s, except PWB for which we were provided with a 1-s sample time, which is expected to be the limit of the instrumental response.

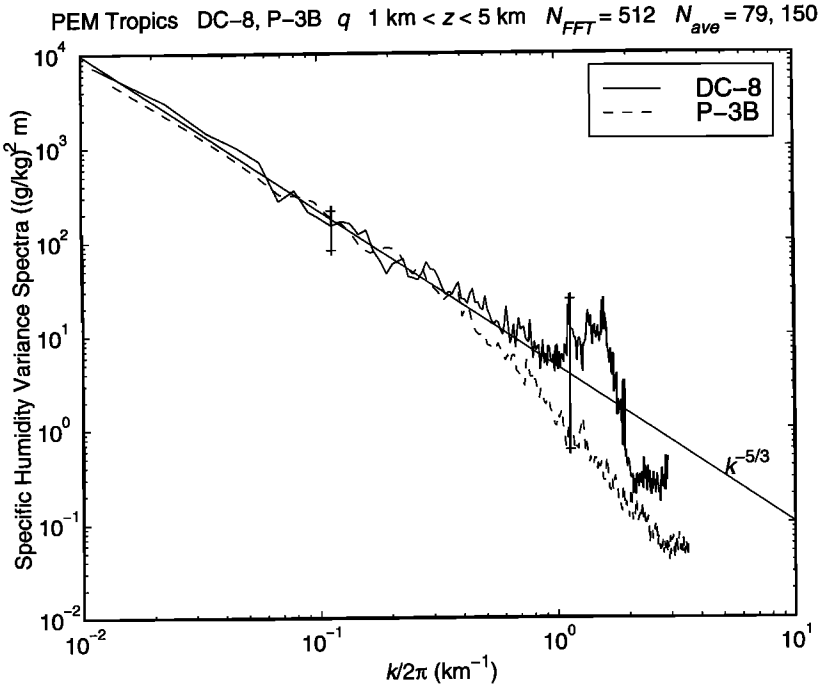

Figure 9. Same as Figure 8, except for an altitude range of 1–5 km.

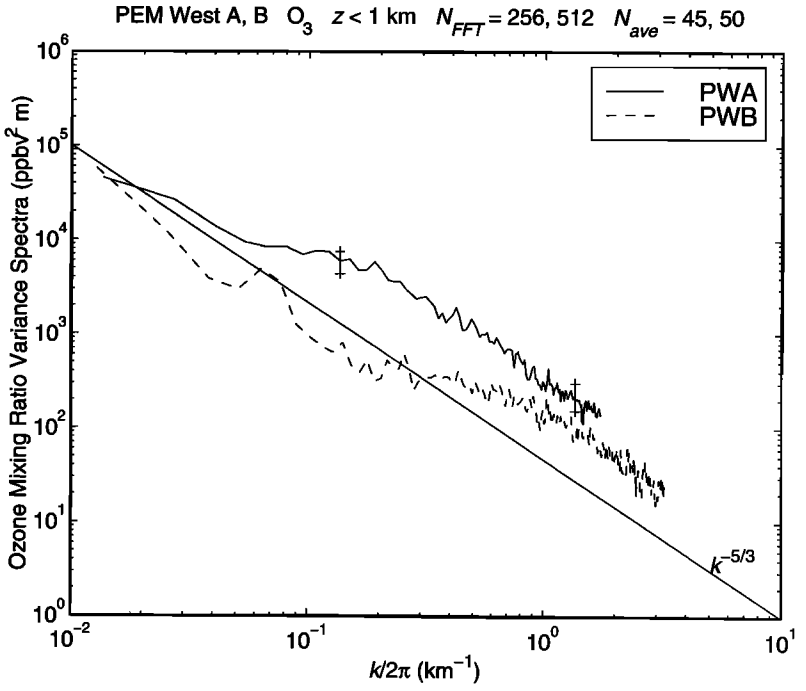

Figure 10. Same as Figure 6, except that the data type is ozone.

Time gaps due to real-time instrumental calibration also made fewer 100-km segments available. Here we plot PWB versus PTD spectra to compare the results of the different resolutions. We chose the 5–11-km range because it had the maximum number of spectra for averaging. Methane mixing ratio spectra are shown in Figure 12, carbon monoxide spectra are shown in Figure 13, and carbon dioxide spectra are shown in Figure 14. We would expect methane and carbon dioxide to have been excellent tracers because of their long lifetimes, and especially in the upper troposphere because the sources were far away at ground level. (Ozone, however, had sources on the ground, in the stratosphere, and in between (lightning).) And we do see that the consistency of their spectra were good across the different campaigns and platforms. The leveling off of the

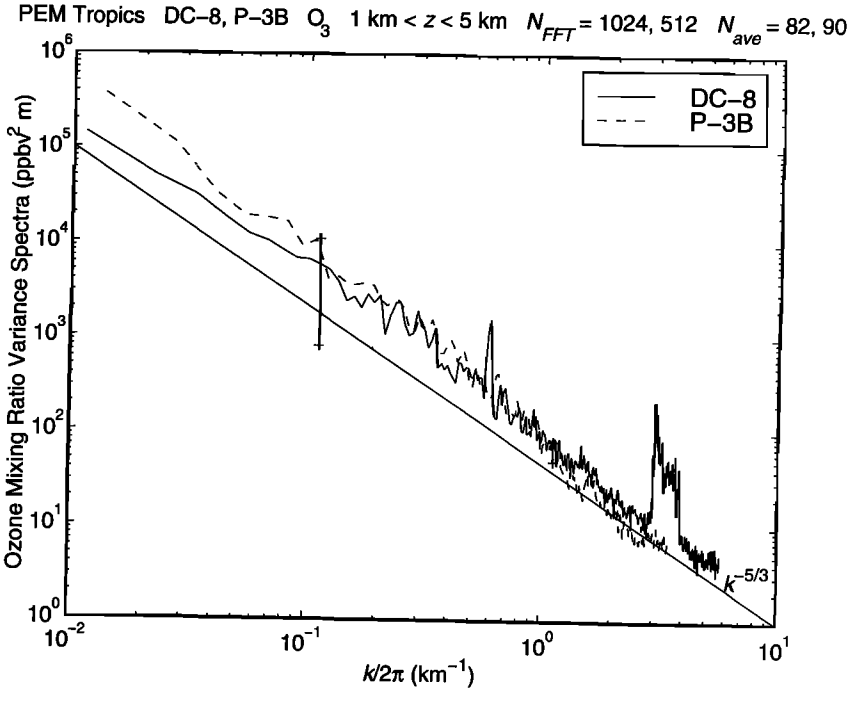

Figure 11. Same as Figure 10, except for an altitude range of 1–5 km.

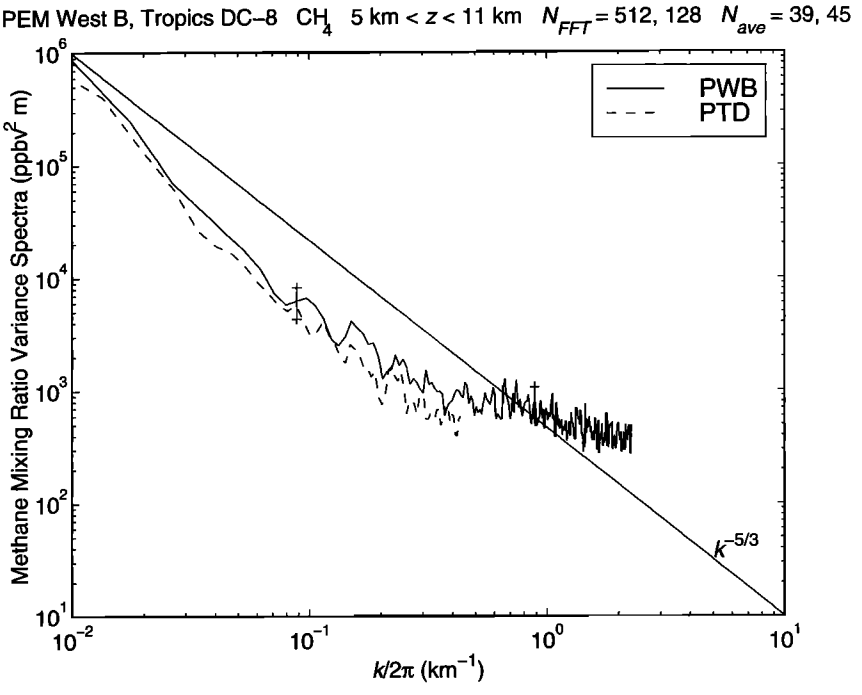

Figure 12. Horizontal wavenumber variance spectra of methane mixing ratio for PWB (solid line) and PTD (dashed line) data. The title above the plot gives the campaign names, data type, altitude range, FFT lengths, and the number of spectral averages for the PWB and PTD data, respectively. See Figure 4 caption for further explanations.

PWB methane, carbon monoxide, and carbon dioxide mixing ratio spectra at $k/(2\pi) > 0.4$ km^{-1} was probably the instrumental noise floor because it happened consistently at the same power level respectively for each species.

Since plotting and displaying all spectra calculated are not possible in journal paper format, we have summarized the results instead by compiling in tables the two main spectral parameters, power and slope, versus altitude and latitude. As we have seen above, there were

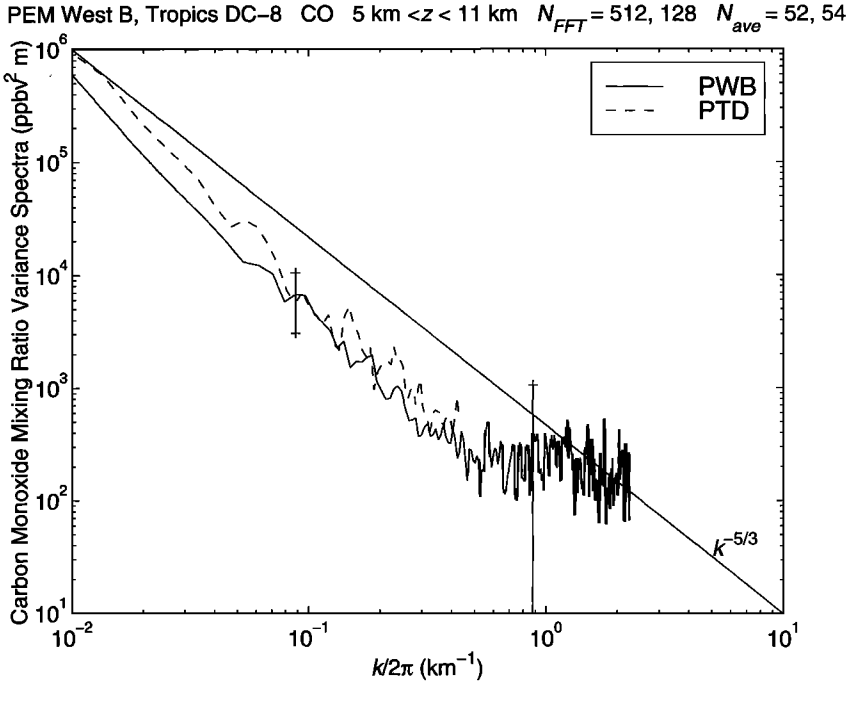

Figure 13. Same as Figure 12, except that the data type is carbon monoxide mixing ratio.

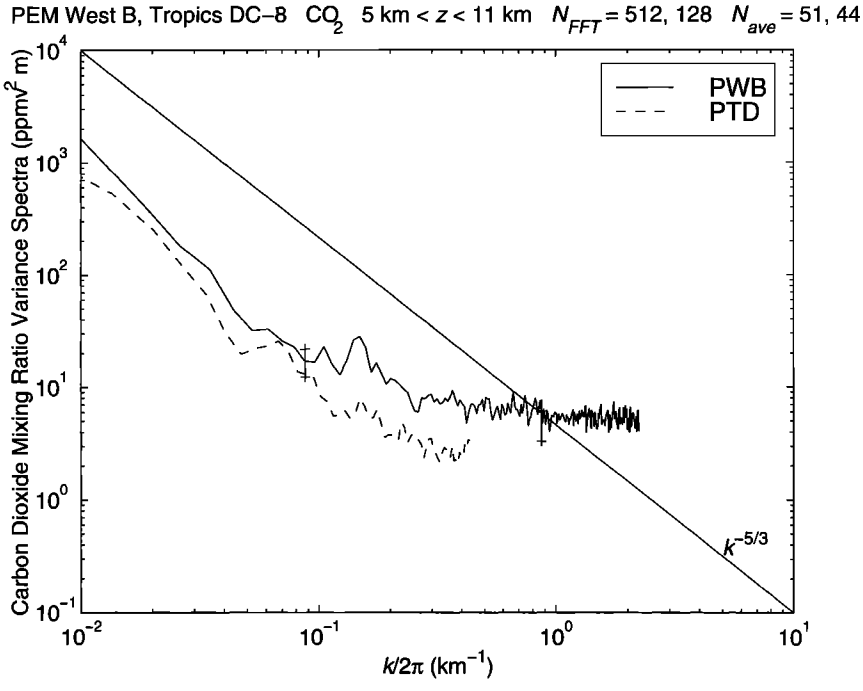

Figure 14. Same as Figure 12, except that the data type is carbon dioxide mixing ratio.

instrumental and data processing artifacts and the hitting of noise floors at high wavenumbers in some of the measurements. Also, some spectra had $k/(2\pi)$ lower limits that did not quite reach the nominal target of 0.01 km^{-1}. Therefore we took the spectral integration and slope fitting over the range 0.0167 km^{-1} < $k/(2\pi)$ < 0.167 km^{-1} (corresponding to 6–60 km in wavelength). To determine the slope, we performed a least squares fit of the spectrum in log-log coordinates to a straight line. The input error in one dimension was the standard deviation divided by the square root of the number of spectral averages, while the input error in the other dimension was the half-width half-maximum of the Hann window spectral power function. The resulting uncertainties in the fitted slopes are given in the tables. We also kept track of the goodness-of-fit parameter, Q, which was the probability that a value of chi-square as poor as the value for the fit should have occurred by chance. In the tables we have flagged slope values that had $Q < 0.1$ to alert the reader that a straight line may not have been a good model for the log-log spectrum in that case.

In making comparisons, one must realize that there were other variables besides altitude and latitude. The PWA and PWB campaigns were conducted in the northwestern Pacific, while the PT flights were mainly in the central and southeastern Pacific. PWA was held in the fall, while PWB was in the spring. In some cases (like ozone), different instruments and data processing were used. On one hand, these differences made the comparison of results difficult, but, on the other hand, if a certain pattern emerged regardless of the differences, then we could have more confidence that the pattern was more universal than merely the characteristic of a certain place, time, instrument, or data processing technique.

Tables 3 and 4 list spectral power versus altitude. Some things to note are (1) there was a tendency for MBL values of horizontal velocity, potential temperature, and ozone to be lower than the free tropospheric values, (2) above the MBL there was no systematic change with height in any of the spectral power quantities except for specific humidity, (3) above the MBL the specific humidity spectral powers decreased with height, (4) the PWA specific humidity spectral powers were much higher than for the other campaigns, and (5) from the surface up to 5 km, PTD chemical tracer spectral powers were the lowest of the four campaigns.

Tables 5 and 6 list log-log spectral slope versus altitude. Here we note that (1) the horizontal velocity spectral slopes tended to be shallower in the MBL than in the free atmosphere, (2) the horizontal velocity spectral slopes above the MBL were generally close to −5/3 but in some cases were slightly steeper or shallower by amounts greater than the uncertainty values, (3) the potential temperature spectral slopes at all heights encompassed −5/3 within the bounds of the error bars, (4) the specific humidity spectral slopes were quite variable with slopes that were significantly steeper than −5/3 in some cases, (5) the ozone spectral slopes were generally close to −5/3 but in some cases were slightly steeper or shallower by amounts greater than the uncer-

Table 3. Spectral Power of Horizontal Wind, Potential Temperature, and Specific Humidity Versus Altitude for Horizontal Wavelength Between 6 and 60 km

Height	Mission	P_u, $m^2\ s^{-2}$	P_v, $m^2\ s^{-2}$	P_θ, K^2	P_q, $10^{-3}\ g^2\ kg^{-2}$
< 1 km	PWA	0.24 ± 0.02 [45]	0.32 ± 0.06 [45]	0.058 ± 0.027 [56]	1500 ± 1100 [50]
	PWB	0.32 ± 0.03 [62]	0.54 ± 0.10 [62]	0.032 ± 0.005 [62]	38 ± 5 [55]
	PTD	0.20 ± 0.02 [54]	0.16 ± 0.02 [54]	0.017 ± 0.002 [54]	55 ± 8 [54]
	PTP	...	...	0.018 ± 0.003 [85]	110 ± 20 [85]
1–5 km	PWA	0.29 ± 0.03 [65]	0.38 ± 0.05 [65]	0.061 ± 0.008 [72]	6000 ± 3700 [72]
	PWB	0.39 ± 0.03 [116]	0.46 ± 0.05 [116]	0.082 ± 0.008 [116]	120 ± 40 [108]
	PTD	0.38 ± 0.04 [84]	0.31 ± 0.03 [84]	0.088 ± 0.015 [84]	130 ± 20 [79]
	PTP	...	...	0.038 ± 0.003 [151]	110 ± 20 [150]
5–11 km	PWA	0.41 ± 0.03 [212]	0.48 ± 0.03 [212]	0.044 ± 0.003 [220]	11 ± 1 [139]
	PWB	0.34 ± 0.02 [309]	0.41 ± 0.02 [309]	0.079 ± 0.006 [309]	0.43 ± 0.07 [283]
	PTD	0.31 ± 0.02 [320]	0.36 ± 0.02 [320]	0.042 ± 0.003 [320]	4.2 ± 0.6 [310]
	PTP	...	...	0.040 ± 0.003 [203]	24 ± 3 [199]
> 11 km	PWA	0.45 ± 0.04 [49]	0.61 ± 0.12 [49]	0.15 ± 0.02 [58]	...
	PWB	0.50 ± 0.07 [19]	0.47 ± 0.07 [19]	0.10 ± 0.02 [19]	3.1[a] ± 0.6[a] [17]
	PTD	0.22 ± 0.02 [26]	0.24 ± 0.03 [26]	0.023 ± 0.004 [26]	6.4[a] ± 2.2[a] [23]
	PTP	...	...	...	...

Numbers in square brackets denote the number of spectra averaged. The uncertainty figures are the standard deviation divided by the square root of the number of spectral averages for each spectral bin, which were then carried through the summation process. The ellipses indicate no data.
[a] $10^{-6}\ g^2\ kg^{-2}$.

tainty values, (6) the carbon monoxide spectral slopes in the MBL were significantly steeper than −5/3, and (7) the carbon dioxide spectral slopes with more than 4 spectral averages encompassed −5/3 within the bounds of the error bars.

Tables 7 and 8 list spectral power versus latitude. Only data from the altitude range of 5–11 km were used to minimize the convolution of any height-dependent effects. Note that (1) the horizontal velocity and potential temperature spectral powers tended to be greater at latitudes higher than 30° compared to latitudes lower than 30°, (2) the specific humidity spectral powers ranged widely with no discernible pattern, and (3) the chemical tracer spectral powers generally increased with latitude.

Tables 9 and 10 list spectral slope versus latitude. Few patterns were discernible in these tables. Again, the spectral slopes for horizontal velocity, potential temperature, and ozone did not depart very far from −5/3, with perhaps a slight preference toward steeper values.

Table 4. Spectral Power of Ozone, Methane, Carbon Monoxide, and Carbon Dioxide Mixing Ratios Versus Altitude for Horizontal Wavelength Between 6 and 60 km

Height	Mission	P_{O3}, $ppbv^2$	P_{CH4}, $ppbv^2$	P_{CO}, $ppbv^2$	P_{CO2}, $10^{-3}\ ppmv^2$
< 1 km	PWA	1.9 ± 0.3 [45]	2.7 ± 0.7 [14]	0.92 ± 0.21 [14]	12 ± 6 [14]
	PWB	0.84 ± 0.27 [50]	4.3 ± 1.1 [12]	4.4 ± 1.7 [13]	12 ± [13]
	PTD	0.22 ± 0.04 [50]	0.80 ± 0.11 [9]	0.38 ± 0.12 [10]	1.7 ± 0.3 [7]
	PTP	0.53 ± 0.13 [53]	16 ± 10 [9]	5.6 ± 3.8 [10]	6.3 ± 3.4 [10]
1–5 km	PWA	6.3 ± 0.7 [70]	7.9 ± 1.7 [19]	4.2 ± 1.3 [19]	11 ± 3 [12]
	PWB	5.6 ± 1.1 [95]	9.6 ± 2.8 [11]	23 ± 10 [22]	26 ± 5 [15]
	PTD	2.5 ± 0.3 [82]	1.3 ± 0.2 [14]	1.3 ± 0.4 [15]	3.2 ± 0.8 [12]
	PTP	6.7 ± 1.6 [90]	3.3 ± 0.5 [34]	3.6 ± 0.8 [37]	11 ± 2 [40]
5–11 km	PWA	6.7 ± 0.5 [190]	7.3 ± 0.9 [55]	3.4 ± 0.4 [55]	7.0 ± 1.0 [51]
	PWB	21 ± 5 [185]	4.8 ± 1.0 [39]	3.5 ± 0.7 [52]	11 ± 2 [51]
	PTD	11 ± 2 [300]	3.3 ± 0.6 [45]	5.6 ± 1.3 [54]	6.2 ± 1.2 [44]
	PTP	3.6 ± 0.4 [141]	8.7 ± 1.2 [41]	6.1 ± 1.0 [49]	12 ± 5 [49]
> 11 km	PWA	19 ± 3 [48]	4.8 ± 1.0 [12]	2.3 ± 0.6 [12]	2.8 ± 0.4 [6]
	PWB	0.16 ± 0.03 [11]	5.3 ± 1.3 [2]	0.66 ± 0.12 [4]	1.6 ± 0.2 [4]
	PTD	5.1 ± 1.6 [26]	0.66 ± 0.22 [6]	0.70 ± 0.23 [5]	5.8 ± 2.0 [4]
	PTP	...	...	...	...

Numbers in square brackets denote the number of spectra averaged. The uncertainty figures are the standard deviation divided by the square root of the number of spectral averages for each spectral bin, which were then carried through the summation process.

Table 5. Spectral Slope of Horizontal Wind, Potential Temperature, and Specific Humidity Versus Altitude for Horizontal Wavelength Between 6 and 60 km

Height	Mission	S_u	S_v	S_θ	S_q
< 1 km	PWA	-0.97 ± 0.22 [45]	-1.3 ± 0.3 [45]	-2.2 ± 0.6 [56]	-2.6 ± 0.6 [50]
	PWB	-0.97 ± 0.16 [62]	-1.3 ± 0.2 [62]	-1.7 ± 0.3 [62]	-1.7 ± 0.3 [55]
	PTD	-1.5 ± 0.2 [54]	-1.6 ± 0.2 [54]	-2.0 ± 0.3 [54]	-1.8 ± 0.3 [54]
	PTP	...	...	-2.1 ± 0.4 [85]	-1.8 ± 0.3 [85]
1–5 km	PWA	-1.2 ± 0.2 [65]	-1.9 ± 0.2 [65]	-1.7 ± 0.2 [72]	-2.7 ± 1.0 [72]
	PWB	-1.5 ± 0.2 [116]	-1.8 ± 0.2 [116]	-1.5 ± 0.2 [116]	-2.9 ± 0.6 [108]
	PTD	-2.0 ± 0.2 [84]	-2.0 ± 0.2 [84]	-1.7 ± 0.3 [84]	-1.7 ± 0.2 [79]
	PTP	...	...	-1.8 ± 0.2 [151]	-1.7 ± 0.3 [150]
5–11 km	PWA	-1.7 ± 0.1 [212]	-1.5 ± 0.2 [212]	-1.6 ± 0.1 [220]	-2.1 ± 0.2 [139]
	PWB	-1.5 ± 0.1[a] [309]	-1.8 ± 0.1[a] [309]	-1.8 ± 0.1 [309]	-2.5 ± 0.3 [283]
	PTD	-2.1 ± 0.1 [320]	-2.1 ± 0.1 [320]	-1.7 ± 0.1 [320]	-1.5 ± 0.2 [310]
	PTP	...	...	-1.6 ± 0.2 [203]	-1.5 ± 0.3 [199]
> 11 km	PWA	-1.8 ± 0.2 [49]	-2.0 ± 0.2 [49]	-1.9 ± 0.2 [58]	...
	PWB	-1.9 ± 0.2 [19]	-1.8 ± 0.2 [19]	-1.9 ± 0.3 [19]	-2.3 ± 0.4 [17]
	PTD	-1.5 ± 0.2 [26]	-2.4 ± 0.3 [26]	-1.7 ± 0.2 [26]	-4.2 ± 0.8 [23]
	PTP	...	...	...	...

Numbers in square brackets denote the number of spectra averaged.
[a]Goodness-of-fit parameter, Q, less than 0.1.

The slopes for methane, carbon monoxide, and carbon dioxide were more widely scattered, but this was not unexpected due to the smaller number of spectra that were available for averaging.

5. Discussion

Above the MBL, our results for horizontal velocity and potential temperature were in general agreement with those from GASP, which showed spectral slopes close to $-5/3$ in the horizontal wavelength range of 2.6–300 km [*Nastrom and Gage*, 1985]. Our results extend the remarkable universality of spectral power and slope evident during GASP (which was mainly confined to the cruising altitudes of commercial airliners) to a range of altitudes throughout the free troposphere. For example, the horizontal velocity spectral powers in Tables 3 and 7 were all within a factor of 3, and the potential temperature spectral slopes across all altitudes could be called $-5/3$ within their uncertainty ranges. Another recent study using an extensive aircraft-acquired data set from the stratosphere indicated a change in spectral slope from $-5/3$ to -3 at a wavelength of $\sim$ 3 km [*Bacmeister et al.*, 1996], with the potential temperature spectral slope a bit steeper than the horizontal velocity spectral slope at wavelengths greater than $\sim$ 10 km. Although

Table 6. Spectral Slope of Ozone, Methane, Carbon Monoxide, and Carbon Dioxide Mixing Ratios Versus Altitude for Horizontal Wavelength Between 6 and 60 km

Height	Mission	S_{O3}	S_{CH4}	S_{CO}	S_{CO2}
< 1 km	PWA	-0.74 ± 0.14 [45]	-2.1 ± 0.4 [14]	-2.6 ± 0.4 [14]	-2.3 ± 1.0 [14]
	PWB	-1.9 ± 0.3 [50]	-1.8 ± 0.3 [12]	-2.6 ± 0.5 [13]	-1.5 ± 0.2 [13]
	PTD	-1.5 ± 0.4 [50]	-1.4 ± 0.3 [9]	-2.9 ± 0.7 [10]	-1.5 ± 0.3 [7]
	PTP	-1.7 ± 0.4 [53]	-2.4 ± 0.7 [9]	-3.0 ± 1.0 [10]	-1.6 ± 0.5 [10]
1–5 km	PWA	-1.4 ± 0.2 [70]	-2.0 ± 0.4 [19]	-2.5 ± 0.5 [19]	-2.0 ± 0.4 [12]
	PWB	-1.9 ± 0.3 [95]	-2.0 ± 0.3 [11]	-2.7 ± 0.6 [22]	-1.5 ± 0.3 [15]
	PTD	-1.6 ± 0.2 [82]	-1.5 ± 0.3 [14]	-1.5 ± 0.2 [15]	-1.5 ± 0.3 [12]
	PTP	-2.2 ± 0.4 [90]	-1.6 ± 0.3 [34]	-1.9 ± 0.3 [37]	-1.7 ± 0.3 [40]
5–11 km	PWA	-1.4 ± 0.1 [190]	-2.6 ± 0.2 [55]	-2.6 ± 0.2 [55]	-1.6 ± 0.1 [51]
	PWB	-2.1 ± 0.3 [185]	-2.0 ± 0.2 [39]	-2.0 ± 0.2 [52]	-1.6 ± 0.2 [51]
	PTD	-1.9 ± 0.2 [300]	-1.6 ± 0.3 [45]	-2.3 ± 0.3 [54]	-1.7 ± 0.2 [44]
	PTP	-1.8 ± 0.2 [141]	-1.1 ± 0.2 [41]	-1.7 ± 0.3 [49]	-1.5 ± 0.3 [49]
> 11 km	PWA	-1.6 ± 0.2 [48]	-2.6 ± 0.4 [12]	-2.4 ± 0.4 [12]	-1.8 ± 0.3 [6]
	PWB	-1.6 ± 0.2 [11]	-2.5 ± 0.2[a] [2]	-2.2 ± 0.4 [4]	-2.8 ± 0.6[a] [4]
	PTD	-2.7 ± 0.6 [26]	-1.6 ± 0.3 [6]	-2.0 ± 0.5 [5]	-3.3 ± 0.9 [4]
	PTP	...	...	...	...

Numbers in square brackets denote the number of spectra averaged.
[a]Goodness-of-fit parameter, Q, less than 0.1.

Table 7. Spectral Power of Horizontal Wind, Potential Temperature, and Specific Humidity Versus Latitude for Horizontal Wavelength Between 6 and 60 km

Latitude	Mission	P_u, $m^2\ s^{-2}$	P_v, $m^2\ s^{-2}$	P_θ, K^2	P_q, $10^{-3}\ g^2\ kg^{-2}$
> 50°N	PWA	0.40 ± 0.07 [23]	0.73 ± 0.11 [23]	0.062 ± 0.015 [24]	16 ± 6 [8]
	PWB	0.53 ± 0.09 [17]	0.44 ± 0.05 [17]	0.15 ± 0.02 [17]	5.5[a] ± 1.5[a] [15]
30°–50°N	PWA	0.63 ± 0.09 [48]	0.72 ± 0.09 [48]	0.046 ± 0.005 [50]	11 ± 2 [31]
	PWB	0.51 ± 0.04 [97]	0.51 ± 0.05 [97]	0.12 ± 0.01 [97]	0.077 ± 0.013 [81]
	PTD	0.31 ± 0.06 [25]	0.34 ± 0.06 [25]	0.023 ± 0.003 [25]	1.1 ± 0.2 [24]
	PTP	...	...	0.095 ± 0.014 [36]	42 ± 5 [39]
10°–30°N	PWA	0.33 ± 0.02 [113]	0.34 ± 0.02 [113]	0.042 ± 0.004 [118]	11 ± 1 [72]
	PWB	0.24 ± 0.01 [143]	0.35 ± 0.02 [143]	0.063 ± 0.007 [143]	0.49 ± 0.13 [141]
	PTD	0.28 ± 0.06 [20]	0.28 ± 0.04 [20]	0.027 ± 0.005 [20]	13 ± 8 [19]
	PTP	...	...	0.029 ± 0.003 [44]	46 ± 12 [40]
10°S–10°N	PWA	0.32 ± 0.03 [28]	0.38 ± 0.05 [28]	0.040 ± 0.004 [28]	12 ± 3 [28]
	PWB	0.25 ± 0.02 [52]	0.36 ± 0.03 [52]	0.018 ± 0.002 [52]	0.99 ± 0.17 [46]
	PTD	0.28 ± 0.03 [71]	0.27 ± 0.02 [71]	0.028 ± 0.003 [71]	6.5 ± 1.6 [71]
	PTP	...	...	0.034 ± 0.006 [43]	17 ± 4 [42]
30°–10°S	PTD	0.31 ± 0.03 [148]	0.35 ± 0.03 [148]	0.049 ± 0.005 [148]	3.3 ± 0.4 [143]
	PTP	...	...	0.025 ± 0.003 [67]	7.9 ± 3.3 [65]
< 30°S	PTD	0.41 ± 0.04 [56]	0.51 ± 0.06 [56]	0.059 ± 0.009 [56]	1.6 ± 0.4 [53]
	PTP	...	...	0.015 ± 0.006 [13]	2.0 ± 0.6 [13]

Numbers in square brackets denote the number of spectra averaged. The uncertainty figures are the standard deviation divided by the square root of the number of spectral averages for each spectral bin, which were then carried through the summation process. Only data from the altitude range of 5–11 km were used.
[a] $10^{-6}\ g^2\ kg^{-2}$.

the spectral power and slope values in the summary tables in section 4 covered the wavelength range of 6–60 km, our full spectral results for horizontal velocity and potential temperature, which covered a range of about 0.5–100 km, did not display such break points, even at altitudes above 11 km. Note that a subset of GASP spectra did have such a break point (at wavelengths of ~ 15 km in the stratosphere and ~ 23 km in the troposphere), over mountainous terrain in high-wind conditions [*Nastrom et al.*, 1987]. If a departure from a −5/3 slope was due to extra energy injected by orographically generated gravity waves, then the lack of a break point in our spectra is consistent with the fact that the PEM flights were conducted over the ocean.

Table 8. Spectral Power of Ozone, Methane, Carbon Monoxide, and Carbon Dioxide Mixing Ratios Versus Latitude for Horizontal Wavelength Between 6 and 60 km

Latitude	Mission	P_{O3}, $ppbv^2$	P_{CH4}, $ppbv^2$	P_{CO}, $ppbv^2$	P_{CO2}, $10^{-3}\ ppmv^2$
> 50°N	PWA	14 ± 3 [22]	...	...	...
	PWB	14 ± 3 [16]	6.4 ± 2.4 [2]	5.1 ± 1.8 [3]	14 ± 4 [3]
30°–50°N	PWA	6.7 ± 1.0 [51]	10 ± 3 [6]	2.5 ± 0.9 [6]	15 ± 7 [6]
	PWB	52 ± 16 [50]	7.3 ± 3.4 [8]	4.5 ± 2.7 [10]	30 ± 11 [9]
	PTD	20 ± 5 [22]	...	2.9 ± 0.4 [4]	9.7 ± 2.2 [3]
	PTP	4.3 ± 0.9 [22]	23 ± 3 [7]	28 ± 5 [8]	42 ± 18 [9]
10°–30°N	PWA	6.0 ± 0.5 [95]	8.8 ± 1.2 [37]	4.1 ± 0.6 [37]	6.9 ± 0.8 [34]
	PWB	7.5 ± 1.7 [78]	4.2 ± 0.6 [21]	3.3 ± 0.6 [23]	6.5 ± 0.9 [24]
	PTD	14 ± 6 [20]	0.87 ± 0.28 [4]	1.1 ± 0.5 [4]	2.8 ± 0.5 [5]
	PTP	4.0 ± 1.0 [22]	8.4 ± 4.0 [10]	1.4 ± 0.5 [14]	5.0 ± 1.4 [13]
10°S–10°N	PWA	3.6 ± 0.3 [22]	1.2 ± 0.1 [12]	1.6 ± 0.3 [12]	2.4 ± 0.2 [11]
	PWB	11 ± 5 [41]	2.6 ± 0.4 [8]	2.8 ± 0.6 [16]	4.8 ± 0.5 [15]
	PTD	2.1 ± 0.2 [69]	1.1 ± 0.2 [7]	0.53 ± 0.09 [9]	1.3 ± 0.1 [6]
	PTP	1.4 ± 0.2 [31]	1.9 ± 0.2 [8]	2.7 ± 1.0 [9]	3.3 ± 0.5 [9]
30°–10°S	PTD	7.6 ± 1.5 [141]	3.0 ± 0.7 [22]	1.2 ± 0.4 [24]	1.3 ± 0.1 [19]
	PTP	4.3 ± 1.0 [55]	5.1 ± 0.9 [14]	1.5 ± 0.3 [15]	2.7 ± 0.5 [15]
< 30°S	PTD	30 ± 9 [48]	6.3 ± 1.9 [12]	21 ± 6 [13]	19 ± 5 [11]
	PTP	5.1 ± 1.3 [11]	16 ± 5 [2]	2.1 ± 0.9 [3]	3.1 ± 1.2 [3]

Numbers in square brackets denote the number of spectra averaged. The uncertainty figures are the standard deviation divided by the square root of the number of spectral averages for each spectral bin, which were then carried through the summation process. Only data from the altitude range of 5–11 km were used.

Table 9. Spectral Slope of Horizontal Wind, Potential Temperature, and Specific Humidity Versus Latitude for Horizontal Wavelength Between 6 and 60 km

Latitude	Mission	S_u	S_v	S_θ	S_q
> 50°N	PWA	-1.8 ± 0.2 [23]	-1.8 ± 0.4 [23]	-1.9 ± 0.3 [24]	-1.7 ± 0.3 [8]
	PWB	-1.7 ± 0.2 [17]	-1.9 ± 0.2[a] [17]	-2.2 ± 0.3 [17]	-2.9 ± 0.5 [15]
30°–50°N	PWA	-2.0 ± 0.2 [48]	-1.8 ± 0.2 [48]	-1.7 ± 0.2 [50]	-2.4 ± 0.4 [31]
	PWB	-1.5 ± 0.1 [97]	-1.7 ± 0.1[a] [97]	-1.9 ± 0.2 [97]	-2.5 ± 0.3 [81]
	PTD	-2.3 ± 0.2 [25]	-2.4 ± 0.2 [25]	-1.9 ± 0.3 [25]	-1.8 ± 0.3 [24]
	PTP	...	...	-1.6 ± 0.2 [36]	-1.4 ± 0.3 [39]
10°–30°N	PWA	-1.6 ± 0.1 [113]	-1.6 ± 0.2 [113]	-1.6 ± 0.1 [118]	-2.0 ± 0.2 [72]
	PWB	-1.8 ± 0.1[a] [143]	-1.9 ± 0.1[a] [143]	-1.8 ± 0.2 [143]	-2.6 ± 0.4 [141]
	PTD	-2.4 ± 0.2 [20]	-2.2 ± 0.2 [20]	-1.8 ± 0.2 [20]	-3.2 ± 1.0 [19]
	PTP	...	...	-1.7 ± 0.3 [44]	-2.1 ± 0.5 [40]
10°S–10°N	PWA	-2.0 ± 0.2 [28]	-1.7 ± 0.2 [28]	-1.7 ± 0.2 [28]	-2.5 ± 0.4 [28]
	PWB	-2.0 ± 0.2[a] [52]	-2.2 ± 0.2[a] [52]	-1.4 ± 0.1 [52]	-2.5 ± 0.4 [46]
	PTD	-2.1 ± 0.2 [71]	-2.2 ± 0.2 [71]	-1.5 ± 0.2 [71]	-1.3 ± 0.3 [71]
	PTP	...	...	-2.2 ± 0.3 [43]	-1.8 ± 0.4 [42]
30°–10°S	PTD	-2.0 ± 0.2 [148]	-2.1 ± 0.2 [148]	-1.7 ± 0.2 [148]	-1.7 ± 0.2 [143]
	PTP	...	...	-1.9 ± 0.3 [67]	-1.5 ± 0.6 [65]
< 30°S	PTD	-2.1 ± 0.2 [56]	-2.4 ± 0.2 [56]	-2.1 ± 0.2 [56]	-2.0 ± 0.4 [53]
	PTP	...	...	-2.2 ± 0.5 [13]	-4.1 ± 0.9 [13]

Numbers in square brackets denote the number of spectra averaged. Only data from the altitude range of 5–11 km were used.
[a]Goodness-of-fit parameter, Q, less than 0.1.

That the data used by *Bacmeister et al.* [1996] were collected over both land and ocean is also consistent with this hypothesis. The situation can also be viewed in the context of the saturated-cascade gravity-wave theory in terms of the cascade "set-up time" [*Dewan*, 1997]. If the gravity waves encountered by the aircraft predominantly emanated from a local source (such as mountains directly beneath the flight path), then the propagating waves would have had less time to cascade from longer to shorter scales before reaching the aircraft than if the waves had originated remotely. The break point, which presumably marks the end of the wave cascade and the beginning of a turbulent regime, then would occur at lower wavenumbers for the local-source case than for the remote-source case. Thus, assuming that gravity-wave sources in our case were purely remote, the wave

Table 10. Spectral Slope of Ozone, Methane, Carbon Monoxide, and Carbon Dioxide Mixing Ratios Versus Latitude for Horizontal Wavelength Between 6 and 60 km

Latitude	Mission	S_{O3}	S_{CH4}	S_{CO}	S_{CO2}
> 50°N	PWA	-1.8 ± 0.3 [22]	...	...	...
	PWB	-2.4 ± 0.3 [16]	-2.6 ± 0.5 [2]	-2.7 ± 0.5 [3]	-2.6 ± 0.4 [3]
30°–50°N	PWA	-1.5 ± 0.1 [51]	-2.9 ± 0.4 [6]	-3.1 ± 0.4 [6]	-2.5 ± 0.3 [6]
	PWB	-2.3 ± 0.4 [50]	-2.5 ± 0.6 [8]	-2.7 ± 0.7 [10]	-2.9 ± 0.9 [9]
	PTD	-2.2 ± 0.4 [22]	...	-2.3 ± 0.2 [4]	-2.0 ± 0.3 [3]
	PTP	-1.8 ± 0.4 [22]	-1.2 ± 0.3 [7]	-1.9 ± 0.3 [8]	-1.7 ± 0.3 [9]
10°–30°N	PWA	-1.3 ± 0.1 [95]	-2.6 ± 0.3 [37]	-2.6 ± 0.3 [37]	-1.7 ± 0.2 [34]
	PWB	-1.8 ± 0.3 [78]	-2.0 ± 0.3 [21]	-2.1 ± 0.3 [23]	-1.3 ± 0.2 [24]
	PTD	-2.6 ± 0.7 [20]	-2.8 ± 0.2 [4]	-1.4 ± 0.2 [4]	-1.7 ± 0.4 [5]
	PTP	-1.7 ± 0.4 [22]	-1.8 ± 0.6 [10]	-1.9 ± 0.6 [14]	-1.5 ± 0.4 [13]
10°S–10°N	PWA	-1.4 ± 0.2 [22]	-2.0 ± 0.2 [12]	-2.6 ± 0.5 [12]	-1.1 ± 0.1 [11]
	PWB	-2.2 ± 0.4 [41]	-2.2 ± 0.4 [8]	-1.8 ± 0.3 [16]	-0.96 ± 0.15 [15]
	PTD	-1.7 ± 0.2 [69]	-1.9 ± 0.3 [7]	-2.0 ± 0.5 [9]	-1.5 ± 0.2[a] [6]
	PTP	-2.1 ± 0.3 [31]	-1.5 ± 0.3 [8]	-1.9 ± 0.5 [9]	-2.2 ± 0.3 [9]
30°–10°S	PTD	-1.8 ± 0.2 [141]	-2.1 ± 0.3 [22]	-2.6 ± 0.5 [24]	-1.1 ± 0.1[a] [19]
	PTP	-2.0 ± 0.4 [55]	-1.5 ± 0.4 [14]	-2.4 ± 0.4 [15]	-1.5 ± 0.3 [15]
< 30°S	PTD	-2.3 ± 0.4 [48]	-2.1 ± 0.3 [12]	-2.4 ± 0.4 [13]	-2.3 ± 0.4 [11]
	PTP	-2.3 ± 0.5 [11]	-2.2 ± 0.7 [2]	-2.3 ± 0.7 [a] [3]	-2.3 ± 0.4[a] [3]

Numbers in square brackets denote the number of spectra averaged. Only data from the altitude range of 5–11 km were used.
[a]Goodness-of-fit parameter, Q, less than 0.1.

cascade would have "pushed" the spectral break point to higher wavenumbers than we were able to measure.

In the upper troposphere our horizontal velocity and potential temperature spectral powers were greater for latitudes higher than 30°, consistent with both GASP and the balloon-based measurements of *Kao and Wendell* [1970]. Thus mesoscale energy appeared to increase in the extratropics where baroclinic instabilities are common and geostrophic adjustments could generate gravity waves at the right wavelengths.

In the MBL the horizontal velocity spectral slopes for a given campaign were shallower than in the free troposphere. It is not surprising that the spectral forms were different from the free tropospheric case. For example, the gravity-wave spectral theories would not be applicable within a convective MBL because the unstable conditions would not support wave propagation. In the MBL, small scales (shorter than the thickness of the mixed surface layer) are expected to be dominated by three-dimensional turbulence, while wind and temperature fluctuations at longer scales probably result from the distribution of convective plumes. Past studies have shown that increased stability reduced the spectral slopes at those longer length scales, while decreased stability extended the $-5/3$ regime to longer and longer scales [*Kaimal et al.*, 1972; *Nicholls and Readings*, 1981]. For a climatological study like ours, a mixture of stability conditions can be expected to produce a composite slope.

The results for specific humidity varied widely. Partly this was due to the different instruments used for the different campaigns and their different sensitivities, accuracies, and response times. However, as noted before, water vapor is not a conservative tracer, and the formation of clouds and precipitation is expected to introduce large changes in humidity variability. This probably explains the drop off in humidity variance with height above the MBL, with fewer cloud patches forming at the higher altitudes. Source variability would have also played a role. The most dramatic example of variability in the humidity spectral power was the much higher values measured during PWA than during the other campaigns. We attribute this difference to PWA having been conducted during the fall in the western Pacific when convective storms and tropical cyclones were active. (In fact, one of the PWA flights sampled airflow in the vicinity of a supertyphoon [*Newell et al.*, 1996a].) As for the GASP results, we cannot make a comparison with them because their spectra were limited to wavelengths greater than 100 km. Although not so useful as a tracer for dynamical studies, the statistics of water vapor distribution as characterized by these spectra should become important as chemists begin to parameterize subgrid-scale processes into their models. Also, the knowledge of spatial variability of water vapor is crucial, especially in the upper troposphere where it can have an impact on the global radiative balance [e.g., *Udelhofen and Hartmann*, 1995]. Because of the nonlinear dependence of the outgoing longwave radiation (OLR) on relative humidity [e.g., *Lindzen*, 1996], increased water vapor horizontal variance in the upper troposphere could actually lead to an increase in OLR (more surface cooling) even though the mean relative humidity value there might remain the same.

The utility of trace chemical species as passive tracers depends on their lifetimes. In the troposphere the lifetimes of ozone, methane, carbon monoxide, and carbon dioxide are about 2 months, 4 years, 4 months, and 5 years, respectively. Ozone lifetime varies strongly with height from less than 1 week in the MBL to $\sim$ 1 year at 10 km, then to shorter times again in the lower stratosphere where heterogeneous reactions can enhance the destruction rate. Source variability can also introduce spatial/temporal variance in the tracer spectra unrelated to the background dynamics. Fortunately, the major sources for these gases (pollution, biomass burning, etc.) were on large land masses far away from the sampling aircraft, especially during the PEM Tropics flights. Ozone had other potential sources such as stratospheric intrusions and lightning, which made it somewhat less reliable as a passive scalar. However, due to the more continuous sampling capability of the measurement devices, there were many more ozone spectra available for averaging, leading to better statistics.

Our ozone spectral slopes did not depart greatly from $-5/3$, which agreed with the stratospheric results of *Bacmeister et al.* [1996], but were clearly different from the GASP tropospheric ozone spectra, which had slopes about -1 for wavelengths below 100 km [*Nastrom et al.*, 1986]. This was very curious because our horizontal velocity and potential temperature spectra agreed better with the GASP spectra. Both *Gage and Nastrom* [1986] and *Bacmeister et al.* [1996] had difficulty explaining the difference in slope between their respective dynamical and tracer spectra. The latter used a model of advection across the mean vertical tracer gradient by gravity waves to get the horizontal wavenumber spectrum for a passive, conservative scalar mixing ratio, χ: $\Phi_\chi(k) = (\bar{\chi}_z/N)^2\Phi_{uv}(k)$, where N is the Brunt-Väisälä frequency, $\bar{\chi}_z$ is the mean vertical scalar gradient, and $\Phi_{uv}(k)$ is the horizontal velocity variance spectrum. Quasi two-dimensional turbulence theory also predicts the same spectral slope, $-5/3$, for the velocity and tracer spectra in the inverse-energy-cascade regime [*Lesieur and Herring*, 1985], so both theories predict that the tracer horizontal wavenumber spectral form should be the same as that for the horizontal velocity. Overall, our results agreed fairly well with this prediction, especially for the tracers ozone and carbon dioxide. However, for the gravity-wave advection model, as *Bacmeister et al.* [1996] pointed out, the vertical gradients of tracer gases are often highly structured due to the existence of thin layers and filaments. The PEM measurements have certainly revealed a plethora of tracer laminae throughout the troposphere [*Newell*

et al., 1996b; *Wu et al.*, 1997; *Stoller et al.*, this issue]. Stochastically, these thin structures themselves introduce a scale dependence, so departures from a strict similarity of spectral forms between velocity and scalar quantities can be expected for the gravity-wave model. This may be one of the reasons for the greater variability of our tracer spectral slopes relative to the velocity spectra.

We had less data on the other trace gases, CH_4, CO, and CO_2, because of calibration data gaps. Spectral slope, the key parameter, ranged fairly widely, but they were clearly steeper than the -1 ozone spectral slope of *Nastrom et al.* [1986]. Carbon dioxide (the tracer with the longest lifetime) had the least-varying spectral slopes across altitudes (Table 6), with values inclusive of $-5/3$ within their uncertainty bounds for spectral averages greater than 4; so, again, the tracer spectral forms generally agreed with the horizontal velocity spectral form.

The general tendency for the tracer spectral powers to increase with latitude confirmed a similar trend observed in the GASP velocity [*Nastrom and Gage*, 1985] and ozone [*Nastrom et al.*, 1986] data. The consistency of our results across the different species, instruments, and platforms gave us an extra measure of confidence in our spectral trends. In light of the similarity of spectral forms between the dynamical spectra and the tracer spectra, the latitudinal trend in the tracer variance was also probably the result of a similar trend in the velocity spectral power.

6. Summary

Our tabulation of the horizontal wavenumber spectral parameters for wavelength regime 6–60 km of horizontal velocity, potential temperature, specific humidity, O_3, CH_4, CO, and CO_2 showed that in the free troposphere their slopes generally did not depart greatly from $-5/3$. Also, in the free troposphere, there was no systematic change of spectral power with height for any of the quantities except for specific humidity, which decreased with height. In the altitude range 5-11 km, the spectral powers of horizontal velocity, potential temperature, and the chemical tracer mixing ratios were generally greater at latitudes higher than 30° compared to latitudes lower than 30°.

Comparisons with previous large-scale aircraft measurement programs yielded the curious result that our horizontal velocity and potential temperature spectra agreed with the GASP data [*Nastrom and Gage*, 1985], whereas our ozone spectra matched the ER-2 results [*Bacmeister et al.*, 1996] better. The persistence of a near $-5/3$ slope for both the dynamical and tracer spectra in our data was consistent with both a gravity-wave advection model [e.g., *Bacmeister et al.*, 1996, p. 9459] and quasi two-dimensional turbulence theory [*Lesieur and Herring*, 1985]. The results from the two previous aircraft studies mentioned in this section were not consistent with either model and were difficult to explain.

In this study we did not observe slopes considerably steeper than $-5/3$ in the horizontal velocity spectra that would be consistent with buoyancy-modified three-dimensional turbulence. In general our results were consistent with the gravity-wave theories [e.g., *Gardner*, 1994; *Dewan*, 1997] and quasi two-dimensional turbulence [*Gage*, 1979; *Lilly*, 1983; *Mahalov et al.*, 1998]. In subsequent papers we will analyze the relationships between the various spectral quantities to address the question of what processes generate the observed wavenumber spectra as well as perform case studies during specific sets of ambient conditions. In particular, for the next article, we will examine Doppler-shifting effects on the velocity spectra and check for polarization relations between u and v using Stokes parameter analysis. Thus, in the second paper of this series, we will focus on comparing the predictions of the gravity-wave and quasi two-dimensional turbulence theories with observationally derived quantities.

Acknowledgments. We would like to thank the flight crews for their hard work on all the campaigns. JYNC would like to acknowledge Drs. Ed Dewan, Greg Nastrom, and Tom VanZandt for helpful discussions. This work was funded in part by NASA grants NAG1-1758 and NAG1-1901.

References

Anderson, B. E., G. L. Gregory, J. E. Collins Jr., G. W. Sachse, T. J. Conway, and G. P. Whiting, Airborne observations of the spatial and temporal variability of tropospheric carbon dioxide, *J. Geophys. Res.*, *101*, 1985–1997, 1996.

Bacmeister, J. T., S. D. Eckermann, P. A. Newman, L. Lait, K. R. Chan, M. Loewenstein, M. H. Proffitt, and B. L. Gary, Stratospheric horizontal wavenumber spectra of winds, potential temperature, and atmospheric tracers observed by high-altitude aircraft, *J. Geophys. Res.*, *101*, 9441–9470, 1996.

Bolgiano, R., Structure of turbulence in stratified media, *J. Geophys. Res.*, *67*, 3015–3023, 1962.

Brasseur, G. P., J.-F. Müller, and C. Granier, Atmospheric impact of NO_x emissions by subsonic aircraft: A three-dimensional model study, *J. Geophys. Res.*, *101*, 1423–1428, 1996.

Clough, P. N., and B. A. Thrush, Mechanism of chemiluminescent reaction between nitric oxide and ozone, *Trans. Faraday Soc.*, *63*, 915–925, 1967.

Collins, J. E., G. W. Sachse, B. E. Anderson, R. C. Harriss, K. B. Bartlett, S. T. Sandholm, L. O. Wade, L. G. Burney, and G. F. Hill, Airborne nitrous oxide observations over the western Pacific Ocean: September-October 1991, *J. Geophys. Res.*, *101*, 1975–1984, 1996.

Dewan, E., Saturated-cascade similitude theory of gravity wave spectra, *J. Geophys. Res.*, *102*, 29,799–29,817, 1997.

Dewan, E. M., Stratospheric wave spectra resembling turbulence, *Science*, *204*, 832–835, 1979.

Dewan, E. M., Similitude modeling of internal gravity wave spectra, *Geophys. Res. Lett.*, *18*, 1473–1476, 1991.

Dewan, E. M., The saturated-cascade model for atmospheric gravity wave spectra, and the wavelength-period (W-P) relations, *Geophys. Res. Lett.*, *21*, 817–820, 1994.

Edouard, S., B. Legras, F. Lefevre, and R. Eymard, The

effect of small-scale inhomogeneities on ozone depletion in the Arctic, *Nature, 384*, 444–447, 1996.

Gage, K. S., Evidence for a $k^{-5/3}$ law inertial range in mesoscale two-dimensional turbulence, *J. Atmos. Sci., 36*, 1950–1954, 1979.

Gage, K. S., and G. D. Nastrom, Spectrum of atmospheric vertical displacements and spectrum of conservative scalar passive additives due to quasi-horizontal atmospheric motions, *J. Geophys. Res., 91*, 13,211–13,216, 1986.

Gardner, C. S., Diffusive filtering theory of gravity wave spectra in the atmosphere, *J. Geophys. Res., 99*, 20,601–20,622, 1994.

Gardner, C. S., and N. F. Gardner, Measurement distortion in aircraft, space shuttle, and balloon observations of atmospheric density and temperature perturbation spectra, *J. Geophys. Res., 98*, 1023–1033, 1993.

Gardner, C. S., C. A. Hostetler, and S. J. Franke, Gravity wave models for the horizontal wave number spectra of atmospheric velocity and density fluctuations, *J. Geophys. Res., 98*, 1035–1049, 1993.

Gibson, C. H., Kolmogorov similarity hypotheses for scalar fields: Sampling intermittent turbulent mixing in the ocean and galaxy, in *Turbulence and Stochastic Processes: Kolmogorov's Ideas 50 Years On*, edited by J. C. Hunt, O. M. Phillips, and D. Williams, pp. 149–164, Royal Society of London, London, 1991.

Hoell, J. M., D. D. Davis, S. C. Liu, R. E. Newell, M. Shipham, H. Akimoto, R. J. McNeal, R. J. Bendura, and J. W. Drewry, Pacific Exploratory Mission West-A (PEM West-A): September-October 1991, *J. Geophys. Res., 101*, 1641–1653, 1996.

Hoell, J. M., D. D. Davis, S. C. Liu, R. E. Newell, H. Akimoto, R. J. McNeal, and R. J. Bendura, The Pacific Exploratory Mission-West, Phase B: February-March 1994, *J. Geophys. Res., 102*, 28,223–28,239, 1997.

Hoell, J. M., D. D. Davis, D. J. Jacob, M. O. Rodgers, R. E. Newell, H. E. Fuelberg, R. J. McNeal, J. L. Raper, and R. J. Bendura, Pacific Exploratory Mission in the tropical Pacific: PEM-Tropics A, August-September 1996, *J. Geophys. Res.*, this issue.

Kaimal, J. C., J. C. Wyngaard, Y. Izumi, and O. R. Coté, Spectral characteristics of surface-layer turbulence, *Q. J. R. Meteorol. Soc., 98*, 563–589, 1972.

Kao, S.-K., and L. L. Wendell, The kinetic energy of the large-scale atmospheric motion in wavenumber-frequency space, I, Northern hemisphere, *J. Atmos. Sci., 27*, 359–375, 1970.

Kolmogorov, A. N., The local structure of turbulence in incompressible viscous fluids for very high Reynolds numbers, *Dokl. Akad. Nauk SSSR, 30*, 301–305, 1941.

Lesieur, M., and J. Herring, Diffusion of a passive scalar in two-dimensional turbulence, *J. Fluid Mech., 161*, 77–95, 1985.

Lilly, D. K., Stratified turbulence and the mesoscale variability of the atmosphere, *J. Atmos. Sci., 40*, 749–761, 1983.

Lilly, D. K., and E. L. Petersen, Aircraft measurements of atmospheric kinetic energy spectra, *Tellus, Ser. A, 35*, 379–382, 1983.

Lindzen, R. S., The importance and nature of the water vapor budget in nature and models, in *Climate Sensitivity to Radiative Perturbations: Physical Mechanisms and Their Validation, NATO ASI Series 1, 34*, 51–66, 1996.

Lumley, J. L., The spectrum of nearly inertial turbulence in a stably stratified fluid, *J. Atmos. Sci., 21*, 99–102, 1964.

Mahalov, A., B. Nicolaenko, and Y. Zhou, Energy spectra of strongly stratified and rotating turbulence, *Phys. Rev. E, 57*, 6187–6190, 1998.

McNeal, R. J., J. P. Mugler Jr., R. C. Harriss, and J. M. Hoell Jr., NASA Global Tropospheric Experiment, *Eos Trans. AGU, 64*, 561–562, 1983.

Müller, J.-F., and G. Brasseur, IMAGES: A three-dimensional chemical transport model of the global troposphere, *J. Geophys. Res., 100*, 16,445–16,490, 1995.

Myrup, L. O., Atmospheric measurements of the buoyant subrange of turbulence, *J. Atmos. Sci., 25*, 1160–1164, 1968.

Nastrom, G. D., and K. S. Gage, A climatology of atmospheric wavenumber spectra of wind and temperature observed by commercial aircraft, *J. Atmos. Sci., 42*, 950–960, 1985.

Nastrom, G. D., W. H. Jasperson, and K. S. Gage, Horizontal spectra of atmospheric tracers measured during the Global Atmospheric Sampling Program, *J. Geophys. Res., 91*, 13,201–13,209, 1986.

Nastrom, G. D., D. C. Fritts, and K. S. Gage, An investigation of terrain effects on the mesoscale spectrum of atmospheric motions, *J. Atmos. Sci., 44*, 3087–3096, 1987.

Newell, R. E., et al., Atmospheric sampling of Supertyphoon Mireille with NASA DC-8 aircraft on September 27, 1991, during PEM-West A, *J. Geophys. Res., 101*, 1853–1871, 1996a.

Newell, R. E., Z.-X. Wu, Y. Zhu, W. Hu, E. V. Browell, G. L. Gregory, G. W. Sachse, J. E. Collins Jr., K. K. Kelly, and S. C. Liu, Vertical fine-scale atmospheric structure measured from NASA DC-8 during PEM-West A, *J. Geophys. Res., 101*, 1943–1960, 1996b.

Nicholls, S., and C. J. Readings, Spectral characteristics of surface layer turbulence over the sea, *Q. J. R. Meteorol. Soc., 107*, 591–614, 1981.

Ridley, B. A., F. E. Grahek, and H. G. Walega, A small, high-sensitivity, medium-response ozone detector suitable for measurements from light aircraft, *J. Atmos. Oceanic Technol., 9*, 142–148, 1992.

Shur, G. H., Experimental studies of the energy spectrum of atmospheric turbulence, *Proc. Central Aerolog. Obser. USSR, 43*, 79–90, 1962.

Sparling, L. C., A. R. Douglass, and M. R. Schoeberl, An estimate of the effect of unresolved structure on modeled ozone loss from aircraft observations of ClO, *Geophys. Res. Lett., 25*, 305–308, 1998.

Stickney, T. M., M. W. Shedlov, and D. I. Thompson, Rosemount total temperature sensors, *Tech. Rep. 5755, Rev. B*, 28 pp., Rosemount Inc., Eden Prairie, Minn., 1990.

Stoller, P., et al., Measurements of atmospheric layers from the NASA DC-8 and P-3B aircraft during PEM-Tropics A, *J. Geophys. Res.*, this issue.

Strahan, S. E., and J. D. Mahlman, Evaluation of the SKYHI general circulation model using aircraft N_2O measurements 2. Tracer variability and diabatic meridional circulation, *J. Geophys. Res., 99*, 10,319–10,332, 1994.

Udelhofen, P. M., and D. L. Hartmann, Influence of tropical cloud systems on the relative humidity in the upper troposphere, *J. Geophys. Res., 100*, 7423–7440, 1995.

Weinstock, J., On the theory of turbulence in the buoyancy subrange of stably stratified flows, *J. Atmos. Sci., 35*, 634–649, 1978.

Wu, Z.-X., R. E. Newell, Y. Zhu, B. E. Anderson, E. V. Browell, G. L. Gregory, G. W. Sachse, and J. E. Collins Jr., Atmospheric layers measured from the NASA DC-8 during PEM-West B and comparison with PEM-West A, *J. Geophys. Res., 102*, 28,353–28,365, 1997.

B. E. Anderson, J. D. Barrick, G. L. Gregory, and G. W. Sachse, Mail Stop 483, NASA Langley Research Center, 21 Langley Blvd., Hampton, VA 23681-0001. (e-mail:

b.e.anderson@larc.nasa.gov; j.d.barrick@larc.nasa.gov; g.l.gregory@larc.nasa.gov; g.w.sachse@larc.nasa.gov)

G. M. Albercook and M. A. Carroll, Department of Atmospheric, Oceanic, and Space Sciences, University of Michigan, 2455 Hayward St., Ann Arbor, MI 48109-2143. (e-mail: mcarroll@umich.edu; galber@umich.edu)

J. Y. N. Cho, R. E. Newell, and Y. Zhu, Department of Earth, Atmospheric, and Planetary Sciences, Massachusetts Institute of Technology, 77 Massachusetts Ave., Rm. 54-1823, Cambridge, MA 02139-4307. (e-mail: jcho@pemtropics.mit.edu; newell@newell1.mit.edu; zhu@newell1.mit.edu)

(Received November 19, 1997; revised April 20, 1998; accepted May 27, 1998.)